

## Metallated Graphynes

# Metallated Graphynes as a New Class of Photofunctional 2D Organometallic Nanosheets

Linli Xu<sup>+</sup>, Jibin Sun<sup>+</sup>, Tianhong Tang<sup>+</sup>, Hongyang Zhang<sup>+</sup>, Mingzi Sun, Jianqi Zhang, Jiahua Li, Bolong Huang, Zhengping Wang,\* Zheng Xie,\* and Wai-Yeung Wong\*

**Abstract:** Two-dimensional (2D) nanomaterials are attracting much attention due to their excellent electronic and optical properties. Here, we report the first experimental preparation of two free-standing mercurated graphyne nanosheets via the interface-assisted bottom-up method, which integrates both the advantages of metal center and graphyne. The continuous large-area nanosheets derived from the chemical growth show the layered molecular structural arrangement, controllable thickness and enhanced  $\pi$ -conjugation, which result in their stable and outstanding broadband nonlinear saturable absorption (SA) properties (at both 532 and 1064 nm). The passively Q-switched (PQS) performances of these two nanosheets as the saturable absorbers are comparable to or higher than those of the state-of-the-art 2D nanomaterials (such as graphene, black phosphorus, MoS<sub>2</sub>,  $\gamma$ -graphyne, etc.). Our results illustrate that the two metallated graphynes could act not only as a new class of 2D carbon-rich materials, but also as inexpensive and easily available optoelectronic materials for device fabrication.

## Introduction

Since the discovery of graphene in 2004, the ultra-thin 2D nanomaterials, such as the elemental analogues of graphene (viz. silicene, germanene and phosphorene), black phosphorus (BP), transition metal dichalcogenides (TMDs), topological insulators (TIs), metal oxides, metal hydroxides and boron nitrides,<sup>[1]</sup> have attracted intensive research attention among scientists since they possess unique chemical, optical and physical properties.<sup>[2]</sup> These 2D nanomaterials are generally composed of single or various elements or molecular frameworks with periodic structures, which can be used for a wide range of applications in the electronics/optoelectron-

ics, catalysis, batteries, supercapacitors and sensing platforms.<sup>[1,2d,3]</sup>

Graphynes include graphyne, graphdiyne and graphyne- $n$  ( $n > 2$ ), depending on the number of acetylenic units. Large-area graphdiyne films were isolated successfully in 2010.<sup>[4]</sup> The use of different multi-substituted acetylenic monomers can lead to the construction of a variety of micro-structures of graphynes/graphdianyenes.<sup>[5]</sup> The fascinating structures and properties of graphynes (the 2D allotrope of graphene) make them a promising class of 2D carbon materials.<sup>[6]</sup> In order to develop new types of graphyne-based materials, metal elements as a new form of molecular functionality can be introduced into the framework of graphdianyenes to afford metallated graphynes. The first-principles density functional theory calculations have been used to explore the excellent mechanical, electronic and optical characteristics and thermal stability of N-, B-, P-, Al-, As-, and Ga-graphyne-based 2D lattices.<sup>[7]</sup> However, related research work on the structurally similar metallated graphynes is still in its infancy and bottom-up large-area and free-standing metallated graphynes were never synthesized.<sup>[8]</sup> In a related context, Sun et al. reported that the formation of 2D  $-\text{C}\equiv\text{C}-\text{Au}-\text{C}\equiv\text{C}-$  organometallic networks was observed under high-resolution scanning tunneling microscope through dehalogenative homocouplings of alkynyl bromides on an Au(111) surface at room temperature (RT) and slight annealing to 320 K.<sup>[8a]</sup> Besides, Yang et al. reported the formation of 2D organometallic Ag-bis-acetylide  $-\text{C}\equiv\text{C}-\text{Ag}-\text{C}\equiv\text{C}-$  networks on Ag(111).<sup>[8b]</sup> However, Au-bis-acetylide can be converted into graphdiyne upon further annealing on Au(111), while Ag-bis-acetylide networks keep their structure even at a rather high temperature on Ag(111). Zhang et al. recently described the organometallic honey-

[\*] Dr. L. Xu,<sup>[+]</sup> Dr. H. Zhang,<sup>[+]</sup> M. Sun, Dr. J. Li, Dr. B. Huang, Prof. Dr. W.-Y. Wong  
 Department of Applied Biology and Chemical Technology and Research Institute for Smart Energy, The Hong Kong Polytechnic University (PolyU)  
 Hung Hom, Hong Kong (P. R. China)  
 and  
 PolyU Shenzhen Research Institute  
 Shenzhen 518057 (P. R. China)  
 E-mail: wai-yeung.wong@polyu.edu.hk  
 Dr. J. Sun,<sup>[+]</sup> Prof. Dr. Z. Xie  
 Key Laboratory of Photochemical Conversion and Optoelectronic Materials, Technical Institute of Physics and Chemistry, Chinese Academy of Sciences  
 29 Zhongguancun East Road, Haidian District, Beijing 100190 (P. R. China)

E-mail: zhengxie@mail.ipc.ac.cn

T. Tang,<sup>[+]</sup> Prof. Dr. Z. Wang  
 State Key Laboratory of Crystal Materials and Institute of Crystal Materials, Shandong University  
 Jinan 250100 (P. R. China)  
 E-mail: zpwang@sdu.edu.cn

Dr. J. Zhang  
 National Center for Nanoscience and Technology  
 Beijing 100190 (P. R. China)

[\*] These authors contributed equally to this work.

 Supporting information and the ORCID identification number(s) for the author(s) of this article can be found under:  
 <https://doi.org/10.1002/anie.202014835>.

comb alkynyl-silver networks with a micrometer domain size which were also detected on Ag(111) under ultrahigh vacuum conditions via a gas-mediated surface reaction protocol.<sup>[8c]</sup> The above 2D Au- and Ag-bis-acetylide networks were all observed on the metal substrates (Au or Ag) with small areas of single or few layers and they cannot be physically isolated easily from the substrates and are thus very difficult to be used in devices. So, one of the present challenges for the preparation of metallated graphynes is to develop methods that can afford their large-area and high-quality films. In this work, we demonstrate two new large-area free-standing mercurated graphyne organometallic nanosheets (MGONs) generated at the interface of an aqueous mercuric chloride solution and a hexane solution of each of the triacetylenic ligands. The propensity of  $d^{10}$   $\text{Hg}^{\text{II}}$  ion to form a linear two-coordinate  $-\text{C}\equiv\text{C}-\text{Hg}-\text{C}\equiv\text{C}-$  moiety with alkynyl units makes  $\text{Hg}^{\text{II}}$  alkynyls an attractive building block for molecular wires and organometallic functional materials.<sup>[9]</sup> Besides, the heavy Hg center was selected based on our previous studies for 1D  $\text{Hg}^{\text{II}}$ -polyyenes where their nonlinear optical (NLO) effects can be enhanced by copolymerization of organic polyyenes with  $\text{Hg}^{\text{II}}$  ions.<sup>[10]</sup> The heavy metal effect also typically magnifies the NLO response by enhancement of the intersystem crossing from  $S_1$  to  $T_1$  states in metal-ethynylene-based optical limiters.<sup>[11]</sup> Hence, it is expected that interesting NLO properties will also be observed in the 2D planar counterparts for the MGONs.

2D materials with extensively delocalized  $\pi$ -conjugated architectures are known to provide good building blocks for new NLO materials with tunable properties.<sup>[12]</sup> The 2D materials with periodic structure present NLO responsive properties which are determined by the crystalline structure, possibly based on the Neumann principle.<sup>[13]</sup> They possess the NLO performances which are highly desirable for the device applications, such as optical limiting, pulse shaping, mode locking, signal and image processing, optical switching, data storage and communication.<sup>[2c,d,14]</sup> Among them, low-dimensional nanomaterials can show saturable absorption (SA) properties which are usually used for passively Q-switching or mode-locking.<sup>[2d,3b,12a,14,15]</sup> Q-switching is a technology to generate a pulse with an ultra-short pulse width and a high peak power. Compared with mode-locking, Q-switching can give a laser with a much larger pulse energy (generally by 2 or 3 orders of magnitude). This technique is of practical importance in many areas, such as military, industry, medical treatment and basic scientific research, where compact, reliable and cost-effective nanosecond pulsed lasers are required. The 2D nanomaterials (e.g. graphene,  $\gamma$ -graphyne, BP, TMDs, etc.) have a low saturation intensity which is favorably used as passively Q-switchers.<sup>[13b,14a,15a,16]</sup> The PQS property of graphene was shown to be tunable with variation of the number of layers.<sup>[14a]</sup> However, the state-of-the-art 2D nanomaterials still have their own shortcomings, such as the dark color (for graphene and its derivatives), the complex preparation procedures (for TIs), instability under ambient conditions (for BP) and defects of nanostructures (for TMDs).<sup>[16f]</sup> On the other hand, for the application of these materials in optical devices, it is necessary to dope them into transparent matrices<sup>[2b-d,12a,15b,16a,c]</sup> or prepare large-area con-

tinuous films on the transparent substrates.<sup>[2d,13b,14a,15a,16b]</sup> which is, however, hard to achieve using these 2D materials.<sup>[17]</sup>

Here, the interface-assisted approaches were used to synthesize the MGONs in which the structural and morphological control can be achieved by the spatial arrangement of the molecular precursors in a confined 2D space, which enables the growth of large-area and high-quality continuous 2D structures with low surface roughness, layered molecular arrangement and enhanced  $\pi$ -conjugation.<sup>[8c,18]</sup> Interestingly, we find that MGONs present excellent broadband NLO and high transmission performance in the solid states, which would lead to many promising applications in optical fields. The MGONs can be transferred to the substrates easily and used as saturable absorbers directly. The SA properties of these two MGONs have been realized experimentally, which can be applied as passive Q-switchers at 1064 nm at the optimal thickness. This is the first literature report on free-standing organometallic nanosheets showing the SA properties and realizing the superb PQS performance as compared to the 2D materials under the same testing conditions. Our experimental results reveal that the metallated graphynes with a large area, regular molecular arrangement and unique chemical structure can be obtained easily via the interface-assisted bottom-up method and these 2D materials are promising optical modulators in integrated optoelectronics.

## Results and Discussion

### Synthesis and characterization of mercurated graphyne organometallic nanosheets

The ligands of tris(4-ethynylphenyl)amine (**L1**) (Scheme S1, Figure 1a) and 1,3,5-triethynylbenzene (**L2**) (Figure 1a) were used to synthesize MGONs, **HgL1** (Figure 1b) and **HgL2** (Figure 1c), by the base-catalyzed dehydrohalogenation reactions. Liquid/liquid and gas/liquid interfacial reactions were employed for synthesizing the multi- and few-layer nanosheets, respectively, following slight modifications of the method used for other coordination-driven metal-complex nanosheets derived from bis(pyrrinato)zinc(II) complexes as reported previously by our group.<sup>[18b,c]</sup> A hexane solution of **L1** (1.0 mM) or **L2** (1.0 mM) and an aqueous  $\text{HgCl}_2$  (2.0 mM) were layered, and the reaction system was kept undisturbed for 24 h (see Figures 2a and 3a, respectively). Then, the generation of multi-layer MGONs at the interface was confirmed as a light yellow (**HgL1** nanosheets) or a colorless (**HgL2** nanosheets) continuous film that was deposited onto a substrate such as glass slide, silicon wafer or quartz (Figure S3a) for subsequent characterization. It was found that the thickness of multi-layer **HgL1** and **HgL2** nanosheets can be controlled by changing the concentrations of the ligands and  $\text{HgCl}_2$ . In view of this, the thickness of multi-layer nanosheets was mainly adjusted by changing the concentration of the ligands while the concentration of  $\text{HgCl}_2$  was kept constant at 2 mM in the following experiments. The few-layer MGONs were prepared via the gas/liquid interfacial reaction, in which a dichloromethane solution of **L1** or **L2** (1.0 mM) was layered on the surface of aqueous  $\text{HgCl}_2$

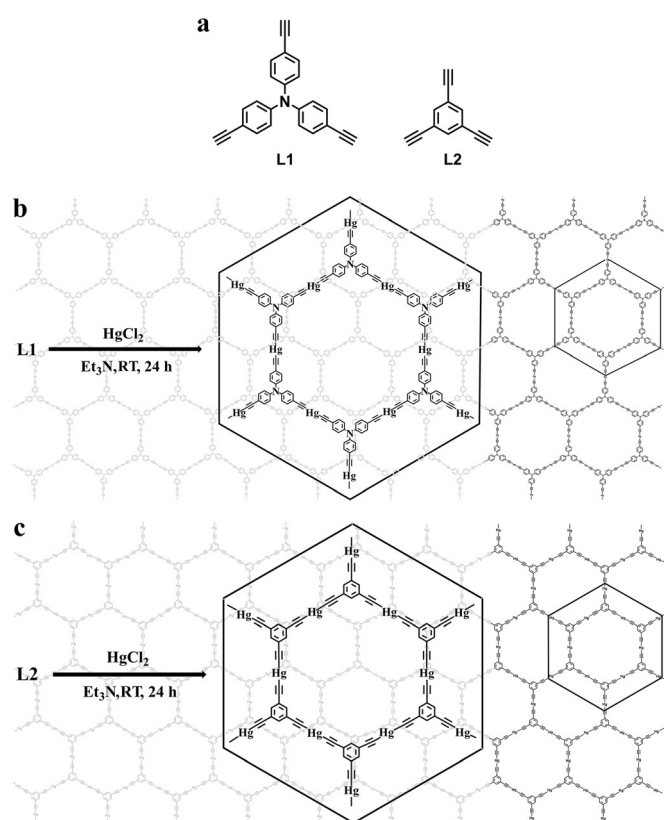


**Figure 1.** Chemical structures of the ligands and mercurated graphyne organometallic nanosheets. a) Molecular structures of L1 and L2. b,c) Synthesis of HgL1 and HgL2 nanosheets.

(2.0 mM). Their thickness can be adjusted by changing the volume of the ligand solution in each case. Few-layer HgL1 or HgL2 nanosheets were then transferred onto Si wafer substrates by using the Langmuir-Schäfer method (Figure S3b) for atomic force microscopy (AFM) observation. Different from the traditional structure of acetylenic nanomaterials, MGONs are a new type of metal-acetylenic nanomaterials.<sup>[5g, 19]</sup> In order to provide the structural models for the HgL1 and HgL2 nanosheets, two control samples of HgL1<sub>M</sub> and HgL2<sub>M</sub> complexes (Scheme S3) were synthesized successfully by using HgCl<sub>2</sub> and L1<sub>M</sub> (Scheme S2 and Figure S4a) or L2<sub>M</sub> under the same basic medium. Their chemical structures were confirmed by nuclear magnetic resonance (NMR) spectroscopy, Fourier-transform infrared (FTIR) spectroscopy (see Figure S4c) and elemental analysis (Table S1). This indicates the feasibility of the synthesis of HgL1 and HgL2 nanosheets.

The photographs of HgL1 and HgL2 nanosheets on the glass slides are presented in Figure 2b and Figure 3b, which display a large film size (> 1 cm). The colors of the nanosheets are consistent with those of the HgL1 and HgL2 bulks, respectively (Figure S5). The morphologies of HgL1 and HgL2 nanosheets were confirmed by scanning electron microscopy (SEM) and transmission electron microscopy (TEM) images, in which both 2D materials showed a sheet and layer structure (Figures 2c, d and 3c, d). AFM images of the few-layer HgL1 and HgL2 nanosheets on the silicon wafer revealed their wrinkle and flat film morphologies, respectively, with the respective film thickness of approximately 17.33 and 40.61 nm (Figures 2e, 3e and Figure S6). In the FTIR spectra of HgL1 and HgL2 nanosheets (Figure S4b), the sharp

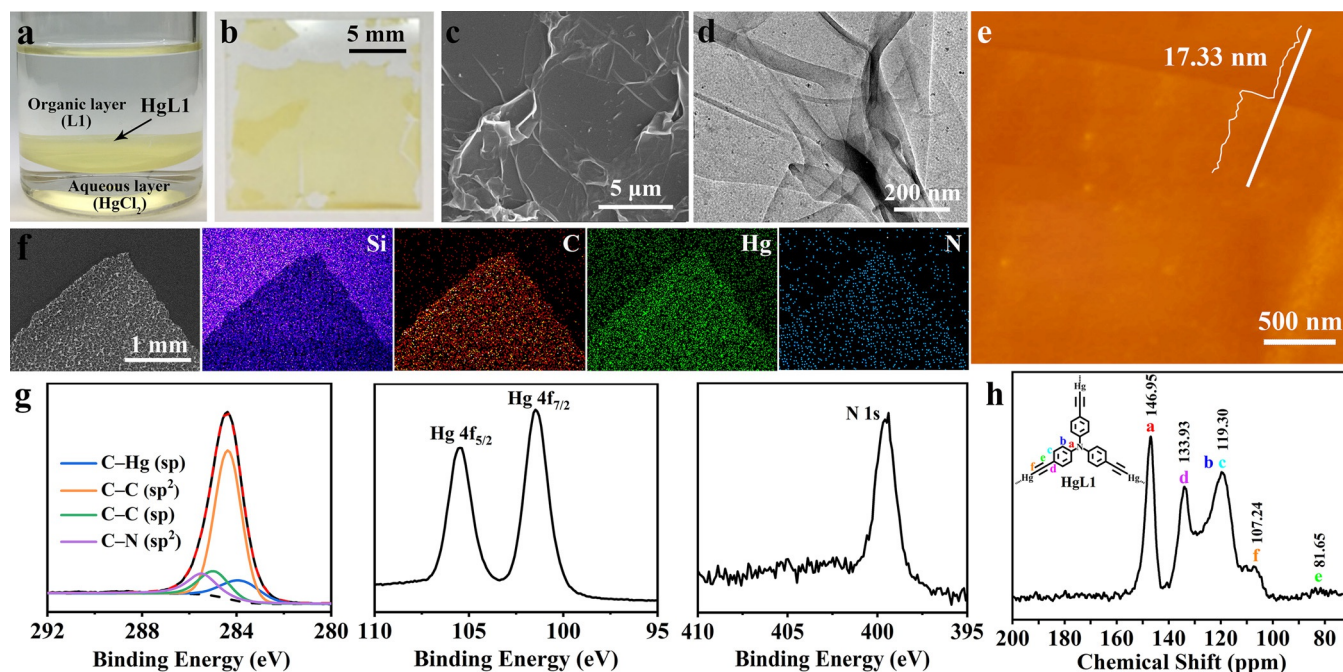


**Figure 2.** The morphology and structure analysis of HgL1 nanosheets. a) Multi-layer HgL1 nanosheets generated at the liquid/liquid interface. b) A photo of HgL1 nanosheets on a slide glass. c) SEM image of HgL1 nanosheets on a Si wafer. d) TEM image of HgL1 nanosheets. e) AFM image and its cross-sectional analysis of the few-layer HgL1 nanosheets on a mica sheet. f) SEM/EDS mapping of HgL1 nanosheets for Si, C, Hg and N elements on a Si wafer. g) XPS analysis of HgL1 nanosheets focusing on C 1s, Hg 4f and N 1s. h) <sup>13</sup>C CP-MAS solid-state NMR spectrum of HgL1 nanosheets.

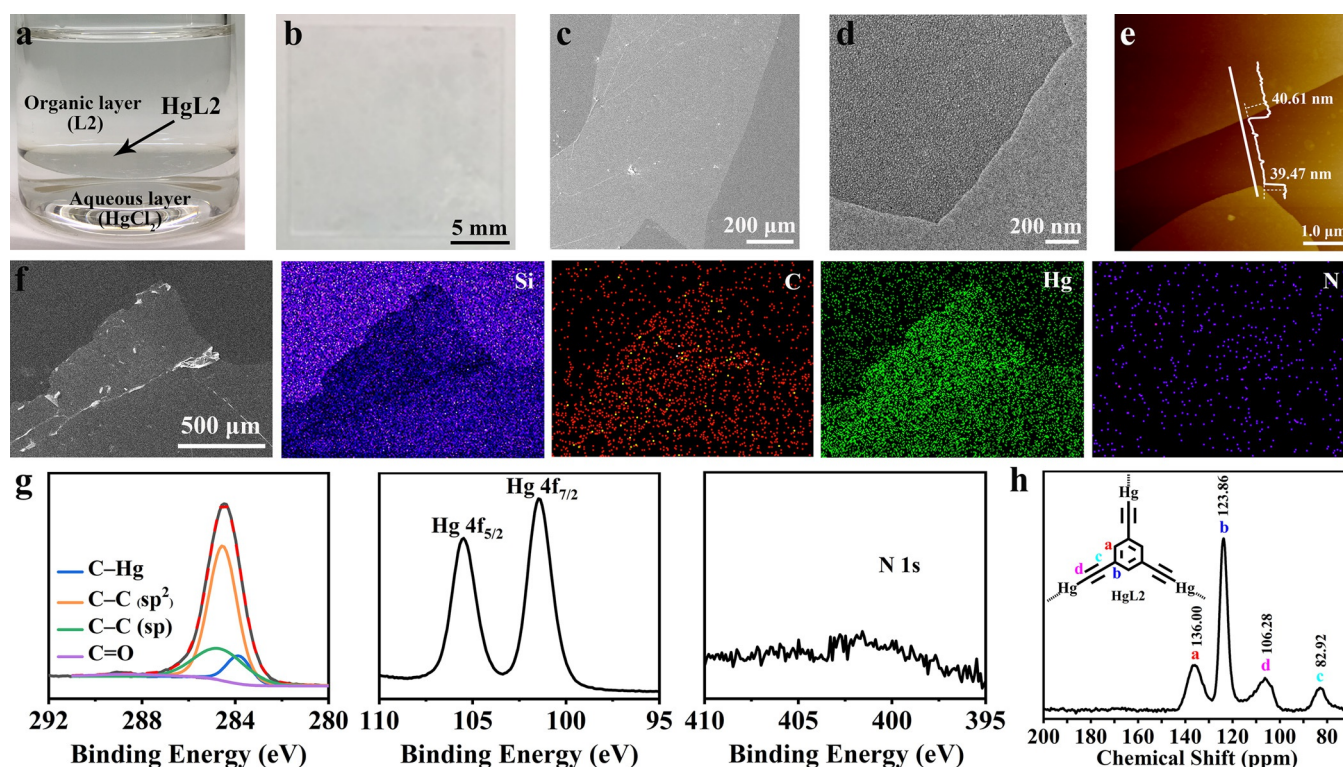


**Figure 3.** The morphology and structure analysis of **HgL2** nanosheets. a) Multi-layer **HgL2** nanosheets generated at the liquid/liquid interface. b) A photo of **HgL2** nanosheets on a slide glass. c) SEM image of **HgL2** nanosheets on a Si wafer. d) TEM image of **HgL2** nanosheets. e) AFM image and its cross-sectional analysis of the few-layer **HgL2** nanosheets on a mica sheet. f) SEM/EDS mapping of **HgL2** nanosheets for Si, C, Hg and N elements on a Si wafer. g) XPS analysis of **HgL2** nanosheets focusing on C 1s, Hg 4f and N 1s. h)  $^{13}\text{C}$  CP-MAS solid-state NMR spectrum of **HgL2** nanosheets.

peaks at  $3310\text{--}3070\text{ cm}^{-1}$  for the  $\equiv\text{C}\text{--H}$  stretching vibrations disappeared, which were observed in the FTIR spectra of **L1** and **L2** (Figure S4a). This indicated that the metal alkynylation reactions occurred and were essentially completed at the interfaces. The main framework of **HgL1** nanosheets consisted of C, N and Hg elements. Energy dispersive X-ray spectroscopy (EDS) with SEM mapping (Figure 2 f) revealed these elements to be spread evenly on the nanosheets. The main framework of **HgL2** nanosheets consisted of C and Hg, which were also spread evenly on the surface of **HgL2** nanosheets and detected by EDS with SEM mapping (Figure 3 f). The elemental composition and chemical bonding of **HgL1** and **HgL2** nanosheets were also confirmed by X-ray photoelectron spectra (XPS). The XPS spectra in Figure S7 display the presence of constitutive C, Hg and N in **HgL1** nanosheets and the C and Hg elements in **HgL2** nanosheets. High-resolution XPS focusing on the C 1s, Hg 4f and N 1s core levels of **HgL1** nanosheets afforded one signal for C 1s and N 1s and two signals for Hg 4f (Figure 2 g). No signal of N 1s appeared from the XPS characterization of **HgL2** nanosheets, which is a clear distinction from the **HgL1** nanosheets (Figure 3 g). Both the C 1s curves of **HgL1** and **HgL2** nanosheets can be deconvoluted into four Gaussian curves (Figures 2 g and 3 g). **HgL1** nanosheets show the curves of C–Hg (sp, 283.8 eV), C–C (sp, 285.0 eV), C–C ( $\text{sp}^2$ , 284.4 eV) and C–N ( $\text{sp}^2$ , 285.5 eV), while **HgL2** nanosheets reveal the curves of C–Hg (sp, 284.1 eV), C–C (sp, 284.8 eV), C–C ( $\text{sp}^2$ , 284.5 eV) and little C=O (288.9 eV, due to the adsorbed  $\text{CO}_2$

on the surface of materials), which indicate the abundance ratio of the  $\text{sp}^2/\text{sp}$  carbons and the successful introduction of Hg ion into the frameworks of graphynes. The abundance ratios of the  $\text{sp}^2/\text{sp}$  carbons are 3 and 1 for **HgL1** and **HgL2** nanosheets, respectively, which is in good agreement with the chemical structures of **HgL1** and **HgL2** nanosheets in Figure 1. The  $^{13}\text{C}$  cross-polarization magic-angle spinning (CP-MAS) NMR spectra of **HgL1** (Figure 2 h) and **HgL2** (Figure 3 h) also confirm the chemical structures of the backbone with a characteristic chemical shift of the  $\equiv\text{C}\text{--Hg}$  at about  $100\text{--}110\text{ ppm}$ ,<sup>[20]</sup> along with the characteristic chemical shifts attributed to the triphenylamine and phenyl groups for **HgL1** and **HgL2**, respectively. These values are in good agreement with those estimated from the nanosheets and the corresponding elemental analysis (Table S1). Both MGONs on a quartz substrate appear transparent under ambient light, because of their weak absorptions in the visible region. The absorption spectrum of **HgL1** nanosheets has two peaks in the ultra-violet (UV) region (peak maximum at 265 and 352 nm, Figure S8a), while the spectrum of **HgL2** nanosheets exhibits two UV absorption peaks (peak maximum at 271 and 376 nm, Figure S8a). The UV-visible spectra of **HgL1<sub>M</sub>** and **HgL2<sub>M</sub>** model complexes (Figure S8b) are consistent with the results of **HgL1** and **HgL2** nanosheets. The thermal stability of the nanosheets was analyzed by thermogravimetry (TG) (Figure S9). The onset decomposition temperatures of **HgL1** and **HgL2** nanosheets are about 260 and 235 °C, respectively, indicating their good thermal stabilities.

## The geometries of HgL1 and HgL2 nanosheets

To gain a deep understanding about the nature of two MGONs (**HgL1** and **HgL2**) with different ligand framework structures, their crystal structures were revealed by using powder X-ray diffraction (PXRD), grazing-incidence small-angle X-ray scattering (GISAXS), density functional theory (DFT)-calculated simulation and high resolution TEM (HRTEM) results. As shown in Figure S10, the diffraction peaks at the  $2\theta$  angles of  $6.4^\circ$ ,  $12.8^\circ$ ,  $20.0^\circ$  and  $25.8^\circ$  for **HgL1** were assigned to (100), (200), (300) and (001) facets and those at  $9.8^\circ$ ,  $20.0^\circ$  and  $27.2^\circ$  for **HgL2** were assigned to (100), (200) and (001) facets, respectively, indicating a long-range order within the  $ab$  plane and the  $\pi$ - $\pi$  stacking between the individual layers. The simulated and experimental PXRD data are almost in agreement, confirming the chemical structures of both nanosheets in Figure 1. The weaker and broader diffraction peaks at  $25.8^\circ$  and  $27.2^\circ$  indicate the interlayer distance of  $\approx 3.45$  and  $3.28$  Å for **HgL1** and **HgL2** nanosheets, respectively. In addition, HRTEM analysis reveals that the interlayer distance is  $\approx 3.43$  Å for **HgL1** (Figure 4a) and  $\approx 3.27$  Å for **HgL2** (Figure 4b), both of which are consistent with those of PXRD and almost like that of graphdiyne ( $3.65$  Å), graphene ( $3.50$  Å) and graphite ( $3.35$  Å).<sup>[21]</sup> 2D GISAXS was also used to study the crystallinity and packing structure of the organometallic nanosheets.<sup>[22]</sup> Here, at the optimal conditions, **HgL1** nanosheets

which were generated by **L1** at a concentration of  $0.75$  mM and  $150^\circ\text{C}$  annealing for  $1$  h were named as **HgL1-0.75-150** and **HgL2** nanosheets which were generated by **L2** at a concentration of  $1.0$  mM and  $150^\circ\text{C}$  annealing for  $1$  h were named as **HgL2-1.0-150**. Figure 4c and d presents the 2D GISAXS pattern of **HgL1-0.75-150** and **HgL2-1.0-150** nanosheets, respectively. To quantify the scattering data, the corresponding out of plane and in plane cuts are given in Figure S11. The 2D GISAXS patterns of **HgL1-1.0-150** and **HgL2-0.75-150** nanosheets show the layer structure and the same stacking pattern in different orientations of the two nanosheets. From the DFT simulation results, both **HgL1** and **HgL2** crystallize in the space group of  $Cmm2$  with the unit cell parameters of  $a=b=33.13$  Å,  $c=3.45$  Å,  $\alpha=\beta=90^\circ$ ,  $\gamma=120^\circ$  for **HgL1** and  $a=b=21.54$  Å,  $c=3.28$  Å,  $\alpha=\beta=90^\circ$ ,  $\gamma=120^\circ$  for **HgL2**. The DFT-calculated structures of the two nanosheets were investigated and the corresponding parameters are shown in Figure 4e and f and Table S2. From Figure 4e, the apparent wavy structure was observed in **HgL1** nanosheets with the evident rotation of benzene groups. The rotation angles of the benzene groups are  $72.5^\circ$ ,  $46.9^\circ$  and  $17.1^\circ$ , respectively. This periodic wavy structure increases the thickness of the structure to around  $4.30$  Å. The pore size of each unit in **HgL1** nanosheets is about  $33.13$  Å. By contrast, the backbone of **L2** in **HgL2** nanosheets possesses a good coplanarity (Figure 4f). The diameter of each unit and the thickness of one layer in **HgL2** nanosheets are estimated to be about  $21.54$  and  $1.50$  Å, respectively. The porosity of **HgL1** and **HgL2** bulks was investigated by argon adsorption measurement,<sup>[23]</sup> which revealed a Brunauer-Emmett-Teller (BET) surface area of  $183.9$  and  $26.0$   $\text{m}^2\text{g}^{-1}$  and an average pore size of  $\approx 33.17$  and  $21.58$  Å for **HgL1** and **HgL2** bulks (Figure S12), respectively, which agree well with the calculated results of both MGONs (Figure 4e and f).

The electronic and optical properties of the two MGONs were also examined. The iso-surface plots of the highest occupied molecular orbitals (HOMOs)/the lowest unoccupied molecular orbitals (LUMOs) of the MGONs are shown in Figure S13. The driving force of Hg...Hg interactions is revealed based on the HOMO/LUMO distributions.<sup>[9]</sup> The electronic occupation of the LUMO is noted for the Hg atoms while electrons are mostly localized on the C=C or C≡C bonds in the HOMO, leading to the possible interactions between Hg and C≡C to further enhance the mercuriphilic attractions. Moreover, the DFT-calculated Hg-C bond lengths are  $1.99$  Å for **HgL1** and  $2.02$  Å for **HgL2** nanosheets, which are consistent with those in some previously reported structures of Hg-acetylide complexes.<sup>[24]</sup> The two nanosheets show variable band gaps from  $2.14$  to  $3.37$  eV (Table S2). In agreement with the HOMO/LUMO plots, the dominant contribution of the local p-orbitals to the density of states (DOS) and absorption behaviors was observed (Figure S14). These results suggest that the introduction of appropriate  $\pi$ -conjugated unit will lead to the optimized electronic structures. The results of DFT-optimized geometries are in accordance with those of the structures from microscopies and UV-vis absorption data (Figures 2 and 3, Figure S8a).

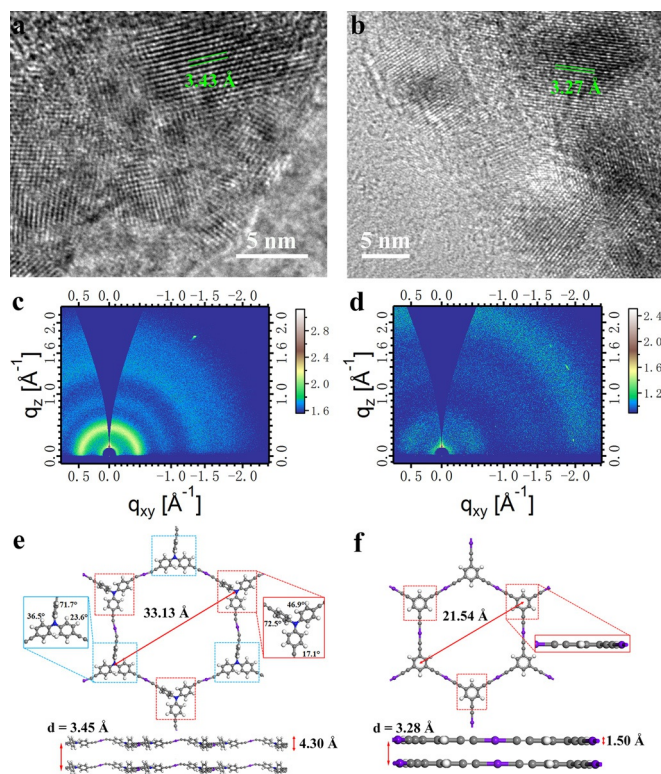


**Figure 4.** HRTEM micrographs, 2D GISAXS patterns and DFT simulation results of MGONs. HRTEM micrographs of a) **HgL1** and b) **HgL2** nanosheets, 2D GISAXS patterns of c) **HgL1-0.75-150** and d) **HgL2-1.0-150** nanosheets and DFT-optimized geometries of e) **HgL1** and f) **HgL2**.

## Nonlinear optical responses of HgL1 and HgL2 nanosheets

To evaluate the NLO properties of **HgL1** and **HgL2** nanosheets, an open-aperture Z-scan technology with nano-second laser under both 532 and 1064 nm was utilized. The as-prepared film at the interface of the two-phase solution was transferred on the quartz plate. **HgL1-0.75–150** and **HgL2-1.0–150** were chosen to examine the NLO properties. The experimental setups and detailed measurement procedures are illustrated in Figure S1 and the selected data are collected in Table S3.

As demonstrated in Figure 5 and Table S3, **HgL1-0.75–150** and **HgL2-1.0–150** nanosheets displayed remarkable SA responses under broadband optical wavelengths of 532 nm and 1064 nm. By exciting the sample at the wavelength of 532 nm for a laser pulse with the input energy ( $E_0$ ) of 11  $\mu\text{J}$ , the modulation depths ( $A_s$ ) of **HgL1-0.75–150** and **HgL2-1.0–150** are 171 % with SA intensity ( $I_s$ ) of 0.40  $\text{J cm}^{-2}$  and 142 % with the  $I_s$  value of 0.34  $\text{J cm}^{-2}$ , respectively. The higher  $A_s$  values indicate the stronger SA properties. The corresponding nonlinear extinction coefficient ( $\beta_{\text{eff}}$ ) values of **HgL1-0.75–150** and **HgL2-1.0–150** nanosheets are 184 and 134  $\text{cm GW}^{-1}$ , respectively. Upon excitation by a laser pulse with the higher  $E_0$  of 184  $\mu\text{J}$  at 1064 nm, the  $A_s$  and  $I_s$  values of **HgL1-0.75–150** are 235 % and 0.78  $\text{J cm}^{-2}$ , respectively, which means that the SA property of **HgL1-0.75–150** nanosheets is better than that of **HgL2-1.0–150** with the  $A_s$  and  $I_s$  values of 150 % and 0.76  $\text{J cm}^{-2}$ , respectively. The corresponding  $\beta_{\text{eff}}$  values of **HgL1-0.75–150** and **HgL2-1.0–150** are 187 and 72  $\text{cm GW}^{-1}$ , respectively. So, the SA performance of **HgL1-0.75–150** is superior to that of **HgL2-1.0–150** at the same  $E_0$  under both 532 nm and 1064 nm. Due to the excellent SA properties, **HgL1-0.75–150** and **HgL2-1.0–150** nanosheets would be potentially good candidates as passively Q-switchers. The SA behavior of the MGONs should be caused by Pauli-

blocking (band-filling effect) due to their molecular frameworks of  $\text{Hg}^{\text{II}}$ -polyyenes with periodic structures.<sup>[25]</sup>

## HgL1 and HgL2 nanosheets as saturable absorbers in passively Q-switched lasers

PQS laser performance was investigated under different conditions, including the variation of thickness of the nanosheets, the use of annealing process and the transmittance of laser output coupler (Figures S2, S15, S16 and S17). At the optimal conditions, the samples of **HgL1-0.75–150** and **HgL2-1.0–150** were also chosen to examine the PQS properties. Being the saturable absorbers, **HgL1-0.75–150** or **HgL2-1.0–150** nanosheets were removed from the resonator and the continuous-wave (CW) Nd:YAG laser at 1064 nm could be obtained. By inserting the saturable absorber into the laser cavity, the PQS operation was realized based on their NLO behaviors. The reproducibility of the experimental results was examined by repeating the same PQS experiments with different samples and the corresponding data listed in Table S4 presented a good reproducibility of the PQS performances. The best results were demonstrated for **HgL1-0.75–150** and **HgL2-1.0–150** nanosheets as shown in Figures 6 and 7, respectively. For the annealed **HgL1-0.75–150** nanosheets and the output coupler at  $T = 20\%$ , the maximum CW and Q-switched output powers were 1.39 W and 50 mW, respectively, at an absorbed pump power of 3.33 W. The output spectrum was recorded and presented as the inset of Figure 6a. The central wavelength was located at 1064 nm, which was in accordance with the strongest emission peak of the Nd:YAG crystal. The stable Q-switched laser operation was achieved at the pump region of 2.01–3.33 W. As shown in Figure 6b and c, with the increase of the absorbed pump power, the pulse width decreased and the repetition frequency, pulse energy and peak power generally presented an increasing trend in each case. The shortest pulse width was

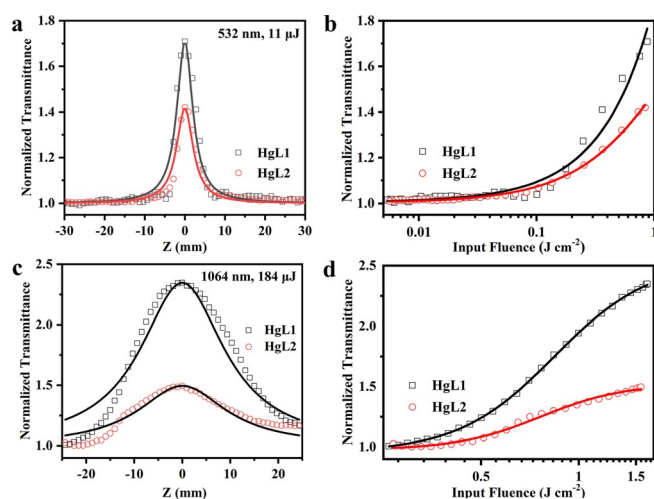


**Figure 5.** NLO properties of MGONs. Open-aperture Z-scan data and theoretically fitted curves (solid curves) of **HgL1-0.75–150** and **HgL2-1.0–150** nanosheets at a) 532 nm with an input energy of 11  $\mu\text{J}$ ; c) 1064 nm with an input energy of 184  $\mu\text{J}$ . Theoretically fitted plots of normalized transmittance vs. incident intensity of **HgL1-0.75–150** and **HgL2-1.0–150** nanosheets at b) 532 nm with an input energy of 11  $\mu\text{J}$ ; d) 1064 nm with an input energy of 184  $\mu\text{J}$ .

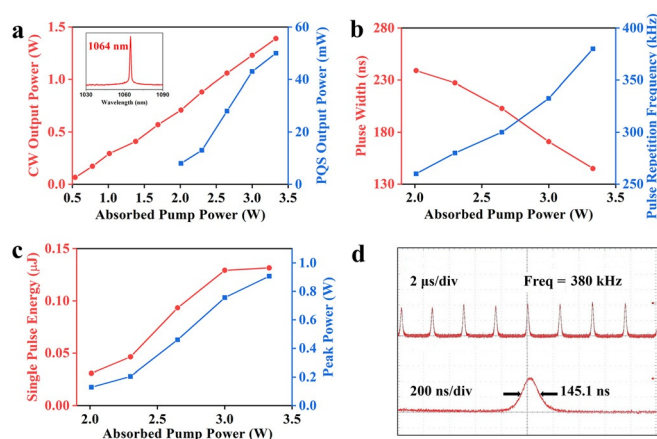


**Figure 6.** Passively Q-switched Nd:YAG laser properties with **HgL1-0.75–150** as the saturable absorber. a) Output power. The inset is the laser emission spectrum. b) Pulse width and repetition frequency. c) Single pulse energy and peak power. d) Pulse train with a repetition rate of 380 kHz and the corresponding pulse profile with a width of 145.1 ns.

145.1 ns, and the largest pulse energy and the highest peak power were 0.132  $\mu\text{J}$  and 0.91 W, respectively. The corresponding pulse train and single pulse profile are shown in Figure 6d. For the annealed **HgL2-1.0** nanosheets and the output coupler at  $T=20\%$  (Figure 7), the maximum CW and Q-switched output powers were 446 and 87 mW, respectively, at an absorbed pump power of 1.39 W. The pump region for stable Q-switched laser operation was 0.59–1.39 W. Just as for the **HgL1-0.75–150** nanosheets, with the increase of the absorbed pump power, the pulse width decreased, and the repetition frequency, pulse energy and peak power generally increased. The shortest pulse width was 439.5 ns, the largest pulse energy was 0.541  $\mu\text{J}$  and the highest peak power was 1.23 W. The corresponding pulse train and single pulse profile are shown in Figure 7d.

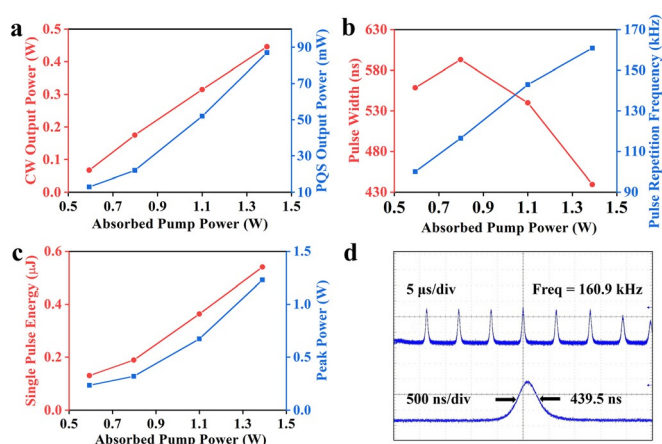


**Figure 7.** Passively Q-switched Nd:YAG laser properties with **HgL2-1.0–150** as the saturable absorber. a) Output power. b) Pulse width and repetition frequency. c) Single pulse energy and peak power. d) Pulse train with a repetition rate of 160.9 kHz and the corresponding pulse profile with a width of 439.5 ns.

The main experimental data from Figures 6 and 7 are summarized in Table S5. For comparison, the PQS performance parameters of 1064 nm solid-state laser of several famous 2D nanomaterials like  $\gamma$ -graphyne, graphene, BP,  $\text{MoS}_2$ ,  $\text{WS}_2$  and  $\text{ReS}_2$  are also listed in Table S5.<sup>[13b,15a,16b,d,e]</sup> It should be noted that the experimental conditions of the data for the nanosheets listed in Table S5 are the same, so that such a comparison has more reference value. It could be seen that the performance of **HgL1** nanosheets is comparable to those of graphene, BP and  $\text{ReS}_2$ . Among the listed materials, **HgL2** nanosheets exhibited the best pulse properties, including the largest single pulse energy and the highest peak power. From the data in Tables S4 and S5, the PQS performance of two MGONs (especially **HgL2**) showed obvious advantages over the  $\gamma$ -graphyne. Recent computational investigations have suggested that the doping of alkali metal atoms into the graphdiyne surface can greatly increase the NLO response which is caused by the intramolecular donor- $\pi$ -acceptor (D- $\pi$ -A) charge transfer mechanism.<sup>[26]</sup> It is conceived that when the mercury ion is polymerized with the multi-substituted alkynyl monomers via  $d\pi$ - $p\pi$  interactions between the Hg *d*

orbital and *p* orbitals of alkyne ligands, the  $\pi$ -electrons are delocalized over the whole framework, which results in the extension of  $\pi$ -conjugation and gives rise to an intramolecular D- $\pi$ -A charge-transfer process. The presence of mercuriphilic interactions in the solid state of the model complexes and the related polyynes<sup>[9]</sup> would promote stronger  $\pi$ - $\pi$  stacking of the frameworks, which facilitates charge transport.<sup>[27]</sup> This result is consistent with that of the DFT calculations. Therefore, the mercurated graphynes can present better NLO properties than that of the  $\gamma$ -graphyne. Thus, the SA effects are improved and the PQS performance of the mercurated graphynes are comparable or higher than those of the representative 2D materials like graphene,  $\gamma$ -graphyne, BP and TMDs.

Nevertheless, the pulse laser performance can be further improved by optimizing the thickness of nanosheets, the type of metal, the nanostructure of ligand as well as the laser design strategy. For the laser design, the pump absorption efficiency of the present Nd:YAG laser crystal is only 50% or so, and a large amount of residual, unabsorbed pump power will cause thermal induced loss in the SA component. So, a Nd:YAG crystal with a high pump absorption efficiency will significantly relieve the thermal effect in the SA component. Besides, other available methods include the anti-reflection (AR) coated on the substrate to decrease the insertion loss of SA, using a pump source with a large fiber core diameter to increase the energy storage ability.

It is worth mentioning that no thermal damage during the PQS examination was observed in the two nanosheets and the output was stable during the laser operation at the highest pump power, which indicates that the MGONs were very stable under strong laser irradiation that is suitable for practical applications. With a flash lamp pumping the Nd:YAG laser, the laser damage thresholds of **HgL1-0.75–150** and **HgL2-1.0–150** nanosheets at 1064 nm were measured to be 657 and 329  $\text{MW cm}^{-2}$ , respectively. In the PQS laser experiments, the highest intracavity power density was estimated to be 21.2 and 28.6  $\text{kW cm}^{-2}$  for **HgL1-0.75–150** and **HgL2-1.0–150** nanosheets, respectively. Both are much lower than their respective laser damage threshold.

## Conclusion

Two MGONs were synthesized as a new kind of metalated acetylenic materials, which were isolated as multi- and few-layers via liquid/liquid and gas/liquid interfacial reactions, respectively. The results of cytotoxicity experiments indicate that the MGONs have relatively low cytotoxicity and virtually no strong toxic effect to human body (Figure S18), adding a weight to their practical value. The NLO properties of the nanosheets were investigated under excitation wavelengths at both 532 and 1064 nm using the Z-scan technique. Interestingly, both nanosheets showed optical switching behavior of SA. Based on the adjustable SA behavior and structure by controlling the concentrations and the types of the ligands (**L1** and **L2**), the PQS properties at the wavelength of 1064 nm were realized with the two nanosheets as saturable absorbers. With the use of the optimal thickness of the

nanosheets, annealing process and output transmittance of a concave mirror, the PQS performance parameters of **HgL1** nanosheets are comparable to those of traditional 2D nanomaterials (such as graphene, BP and MoS<sub>2</sub>, etc.) whereas **HgL2** nanosheets even exhibit better pulse properties, such as the larger single pulse energy (0.541 μJ) and the higher peak power (1.23 W). This work reveals that the metallated graphyne materials can go beyond graphyne and could not only be a new family of stable 2D carbon-rich materials under ambient conditions, but also possess unique properties and application prospects. This may be helpful in the future design of various structures for optoelectronic materials and devices. The chemical nanostructure and macroscopic morphology of the free-standing and high-quality nanosheets can be adjusted by changing the molecular structures (such as the metal chromophores as well as the nanostructure and functional groups in ligands), the concentration of precursors and the preparation conditions in the future. Preliminary study reveals that the work can be readily extended to other transition metals such as the square-planar platinum(II) groups and work along this line is currently underway. Further works are still required to develop other potential applications of these novel large-area metallated graphyne films. These large-area continuous nanosheets with controllable thickness and high transparency can be transferred on the optical glass and other substrates, and can be directly applied as free-standing films in optoelectronic devices. The combination of such outstanding optical properties with good mechanical processability and control of molecular dimensions are beneficial for the design of optoelectronic materials and fabrication of their devices in applications such as nonlinear optics, optical limiting, optical communications and others.

### Acknowledgements

This work was supported by the Science, Technology and Innovation Committee of Shenzhen Municipality (JCYJ20180507183413211), the National Natural Science Foundation of China (NSFC, Grant No. 21905241, 21702214, 61975096 and 21875267), the Hong Kong Research Grants Council (PolyU 153051/17P), the RGC Senior Research Fellowship Scheme (SRFS2021-5S01), the Hong Kong Polytechnic University (1-ZE1C), Guangdong-Hong Kong-Macao Joint Laboratory of Optoelectronic and Magnetic Functional Materials (2019B121205002), Research Institute for Smart Energy (RISE) and the Endowed Professorship in Energy from Ms Clarea Au (847S).

### Conflict of interest

The authors declare no conflict of interest.

**Keywords:** metallated graphynes · nanosheets · optical properties · passively Q-switched laser · saturable absorption

- [1] a) C. L. Tan, X. H. Cao, X.-J. Wu, Q. Y. He, J. Yang, X. Zhang, J. Z. Chen, W. Zhao, S. K. Han, G.-H. Nam, M. Sindoro, H. Zhang, *Chem. Rev.* **2017**, *117*, 6225–6331; b) M. Q. Zeng, Y. Xiao, J. X. Liu, K. Yang, L. Fu, *Chem. Rev.* **2018**, *118*, 6236–6296.
- [2] a) J. S. Bunch, A. M. Van Der Zande, S. S. Verbridge, L. W. Frank, D. M. Tanenbaum, J. M. Parpia, H. G. Craighead, *Science* **2007**, *315*, 490–493; b) K. S. Hu, D. D. Kulkarni, I. Choi, V. V. Tsukruk, *Prog. Polym. Sci.* **2014**, *39*, 1934–1972; c) G. K. Lim, G.-K. Lim, Z.-L. Chen, J. Clark, G. S. G. Roland, W.-H. Ng, H.-W. Tan, R. H. Friend, P. K. H. Ho, L.-L. Chua, *Nat. Photonics* **2011**, *5*, 554–560; d) Q. L. Bao, K. P. Loh, *ACS Nano* **2012**, *6*, 3677–3694.
- [3] a) J. Wu, Y. B. Chen, J. Q. Wu, K. Hippalgaonkar, *Adv. Electron. Mater.* **2018**, *4*, 1800248; b) Z. B. Liang, C. Qu, W. H. Guo, R. Q. Zou, Q. Xu, *Adv. Mater.* **2018**, *30*, 1702891.
- [4] G. X. Li, Y. L. Li, H. B. Liu, Y. B. Guo, Y. J. Li, D. B. Zhu, *Chem. Commun.* **2010**, *46*, 3256–3258.
- [5] a) U. H. F. Bunz, Y. Rubin, Y. Tobe, *Chem. Soc. Rev.* **1999**, *28*, 107–119; b) M. M. Haley, M. L. Bell, J. J. English, C. A. Johnson, T. J. R. Weakley, *J. Am. Chem. Soc.* **1997**, *119*, 2956–2957; c) Q. Zhou, P. J. Carroll, T. M. Swager, *J. Org. Chem.* **1994**, *59*, 1294–1301; d) W. B. Wan, M. M. Haley, *J. Org. Chem.* **2001**, *66*, 3893–3901; e) J. M. Kehoe, J. H. Kiley, J. J. English, C. A. Johnson, R. C. Peterson, M. M. Haley, *Org. Lett.* **2000**, *2*, 969–972; f) C. A. Johnson, Y. Y. Lu, M. M. Haley, *Org. Lett.* **2007**, *9*, 3725–3728; g) C. S. Huang, Y. J. Li, N. Wang, Y. R. Xue, Z. C. Zuo, H. B. Liu, Y. L. Li, *Chem. Rev.* **2018**, *118*, 7744–7803.
- [6] a) K. Kaiser, L. M. Scriven, F. Schulz, P. Gawel, L. Gross, H. L. Anderson, *Science* **2019**, *365*, 1299–1301; b) K. Tahara, Y. Yamamoto, D. E. Gross, H. Kozuma, Y. Arikuma, K. Ohta, Y. Koizumi, Y. Gao, Y. Shimizu, S. Seki, K. Kamada, J. S. Moore, Y. Tobe, *Chem. Eur. J.* **2013**, *19*, 11251–11260; c) Z. H. Li, M. Smeu, A. Rives, V. Maraval, R. Chauvin, M. A. Ratner, E. Borguet, *Nat. Commun.* **2015**, *6*, 6321; d) K. Cocq, N. Saffon-Merceron, Y. Coppel, C. Poidevin, V. Maraval, R. Chauvin, *Angew. Chem. Int. Ed.* **2016**, *55*, 15133–15136; *Angew. Chem.* **2016**, *128*, 15357–15360; e) M. D. Kilde, A. H. Murray, C. L. Andersen, F. E. Storm, K. Schmidt, A. Kadziola, K. V. Mikkelsen, F. Hampel, O. Hammerich, R. R. Tykwinski, M. B. Nielsen, M. D. Kilde, *Nat. Commun.* **2019**, *10*, 3714.
- [7] B. Mortazavi, M. Shahrokhi, M. E. Madjet, T. Hussain, X. Y. Zhuang, T. Rabczuk, *J. Mater. Chem. C* **2019**, *7*, 3025–3036.
- [8] a) Q. Sun, L. L. Cai, H. H. Ma, C. X. Yuan, W. Xu, *ACS Nano* **2016**, *10*, 7023–7030; b) Z. C. Yang, J. L. Gebhardt, T. A. Schaub, T. Sander, J. Schnamsgruber, H. Soni, A. Grling, M. Kivala, S. Maier, *Nanoscale* **2018**, *10*, 3769–3776; c) Y.-Q. Zhang, T. Paintner, R. Hellwig, F. Haag, F. Allegretti, P. Feulner, S. Klyatskaya, M. Ruben, A. P. Seitsonen, J. V. Barth, F. Klappenberger, Y.-Q. Zhang, *J. Am. Chem. Soc.* **2019**, *141*, 5087–5091.
- [9] W.-Y. Wong, *Coord. Chem. Rev.* **2007**, *251*, 2400–2427.
- [10] G. J. Zhou, W.-Y. Wong, Z. Y. Lin, C. Ye, *Angew. Chem. Int. Ed.* **2006**, *45*, 6189–6193; *Angew. Chem.* **2006**, *118*, 6335–6339.
- [11] G. J. Zhou, W.-Y. Wong, *Chem. Soc. Rev.* **2011**, *40*, 2541–2566.
- [12] a) B. P. Biswal, S. Valligatla, M. C. Wang, T. Banerjee, N. A. Saad, B. M. K. Mariserla, N. Chandrasekhar, D. Becker, M. Addicoat, I. Senkovska, R. Berger, D. N. Rao, S. Kaskel, X. L. Feng, *Angew. Chem. Int. Ed.* **2019**, *58*, 6896–6900; *Angew. Chem.* **2019**, *131*, 6970–6974; b) F. Zhang, G. W. Liu, J. J. Yuan, Z. P. Wang, T. H. Tang, S. G. Fu, H. N. Zhang, Z. S. Man, F. Xing, X. G. Xu, *Nanoscale* **2020**, *12*, 6243–6249.
- [13] a) T. Kawasaki, *Prog. Theor. Phys.* **1971**, *46*, 1323–1323; b) R. Zhang, Y. X. Zhang, H. H. Yu, H. J. Zhang, R. L. Yang, B. C. Yang, Z. Y. Liu, J. Y. Wang, *Adv. Opt. Mater.* **2015**, *3*, 1787–1792.

- [14] a) Q. L. Bao, H. Zhang, Y. Wang, Z. H. Ni, Y. L. Yan, Z. X. Shen, K. P. Loh, D. Y. Tang, *Adv. Funct. Mater.* **2009**, *19*, 3077–3083; b) Y. X. Zhang, D. Z. Lu, H. H. Yu, H. J. Zhang, *Adv. Opt. Mater.* **2019**, *7*, 1800886.
- [15] a) H. H. Yu, X. F. Chen, H. J. Zhang, X. G. Xu, X. B. Hu, Z. P. Wang, J. Y. Wang, S. D. Zhuang, M. H. Jiang, *ACS Nano* **2010**, *4*, 7582–7586; b) K. P. Wang, J. Wang, J. T. Fan, M. Lotya, A. O'Neill, D. Fox, Y. Y. Feng, X. Y. Zhang, B. X. Jiang, Q. Z. Zhao, H. Z. Zhang, J. N. Coleman, L. Zhang, W. J. Blau, *ACS Nano* **2013**, *7*, 9260–9267.
- [16] a) H. R. Mu, S. H. Lin, Z. C. Wang, S. Xiao, P. F. Li, Y. Chen, H. Zhang, H. F. Bao, S. P. Lau, C. X. Pan, D. Y. Fan, Q. L. Bao, *Adv. Opt. Mater.* **2015**, *3*, 1447–1453; b) S. X. Wang, H. H. Yu, H. J. Zhang, A. Z. Wang, M. W. Zhao, Y. X. Chen, L. M. Mei, J. Y. Wang, *Adv. Mater.* **2014**, *26*, 3538–3544; c) Z. Q. Luo, Y. Z. Huang, M. Zhong, Y. Y. Li, J. Y. Wu, B. Xu, H. Y. Xu, Z. P. Cai, J. Peng, J. Weng, *J. Lightwave Technol.* **2014**, *32*, 4077–4084; d) G. Zhao, S. Han, A. Z. Wang, Y. Z. Wu, M. W. Zhao, Z. P. Wang, X. P. Hao, *Adv. Funct. Mater.* **2015**, *25*, 5292–5299; e) S. W. Liu, M. X. Wang, S. Y. Yin, Z. Xie, Z. P. Wang, S. Y. Zhou, P. Chen, *Phys. Status Solidi A* **2019**, *216*, 1800837; f) Q. Yang, X. Y. Zhang, Z. X. Yang, X. H. Ren, J. Wang, Q. D. Li, X. L. Cui, X. L. Zhu, *Appl. Phys. Express* **2019**, *12*, 122006.
- [17] Z. L. Chen, Y. Qi, X. D. Chen, Y. F. Zhang, Z. F. Liu, *Adv. Mater.* **2019**, *31*, 1803639.
- [18] a) R. H. Dong, T. Zhang, X. L. Feng, *Chem. Rev.* **2018**, *118*, 6189–6235; b) R. Sakamoto, K. Hoshiko, Q. Liu, T. Yagi, T. Nagayama, S. Kusaka, M. Tsuchiya, Y. Kitagawa, W.-Y. Wong, H. Nishihara, *Nat. Commun.* **2015**, *6*, 7713; c) R. Sakamoto, R. Sakamoto, T. Yagi, K. Hoshiko, S. Kusaka, R. Matsuoka, H. Maeda, Z. Liu, Q. Liu, W.-Y. Wong, H. Nishihara, *Angew. Chem. Int. Ed.* **2017**, *56*, 3526–3530; *Angew. Chem.* **2017**, *129*, 3580–3584; d) T. Tsukamoto, K. Takada, R. Sakamoto, R. Matsuoka, R. Toyoda, H. Maeda, T. Yagi, M. Nishikawa, N. Shinjo, S. Amano, T. Iokawa, N. Ishibashi, T. Oi, K. Kanayama, R. Kinugawa, Y. Koda, T. Komura, S. Nakajima, R. Fukuyama, N. Fuse, *J. Am. Chem. Soc.* **2017**, *139*, 5359–5366; e) T. Kambe, R. Sakamoto, K. Hoshiko, K. Takada, M. Miyachi, J.-H. Ryu, S. Sasaki, J. Kim, K. Nakazato, M. Takata, H. Nishihara, *J. Am. Chem. Soc.* **2013**, *135*, 2462–2465.
- [19] F. Diederich, *Nature* **1994**, *369*, 199–207.
- [20] A. S. Borovik, S. G. Bott, A. R. Barron, *J. Am. Chem. Soc.* **2001**, *123*, 11219–11228.
- [21] Z. Yang, X. Y. Shen, N. Wang, J. J. He, X. D. Li, X. Wang, Z. F. Hou, K. Wang, J. Gao, T. G. Jiu, C. S. Huang, *ACS Appl. Mater. Interfaces* **2019**, *11*, 2608–2617.
- [22] R. Matsuoka, R. Sakamoto, K. Hoshiko, S. Sasaki, H. Masunaga, K. Nagashio, H. Nishihara, *J. Am. Chem. Soc.* **2017**, *139*, 3145–3152.
- [23] a) Y. S. Liu, Y. You, Z. Y. Li, X. Yang, X. Y. Wu, C. Y. Zhao, Y. Xing, R. T. Yang, *J. Hazard. Mater.* **2021**, *407*, 124380; b) Z. Y. Li, Y. S. Liu, H. H. Wang, C.-J. Tsaid, X. Yanga, Y. Xing, C. Z. Zhang, P. Xiao, P. A. Webley, *Chem. Eng. J.* **2018**, *353*, 858–866.
- [24] a) W.-Y. Wong, K. H. Choi, G. L. Lu, Z. Y. Lin, *Organometallics* **2002**, *21*, 4475–4481; b) L. Liu, S. Y. Poon, W.-Y. Wong, *J. Organomet. Chem.* **2005**, *690*, 5036–5048.
- [25] G. Z. Wang, A. A. Baker-Murray, W. J. Blau, *Laser Photonics Rev.* **2019**, *13*, 1800282.
- [26] X. J. Li, S. K. Li, *J. Mater. Chem. C* **2019**, *7*, 1630–1640.
- [27] S. Liu, K. Zhang, J. M. Lu, J. Zhang, H.-L. Yip, F. Huang, Y. Cao, *J. Am. Chem. Soc.* **2013**, *135*, 15326–15329.

Manuscript received: November 5, 2020

Revised manuscript received: January 31, 2021

Accepted manuscript online: February 24, 2021

Version of record online: April 7, 2021